Volcano dome dynamics at Mount St. Helens: Deformation and intermittent subsidence monitored by seismicity and camera imagery pixel offsets

Jacqueline T. Salzer[1] Weston A. Thelen[2,3], Mike R. James[4], Thomas R. Walter[1], Seth Moran[3] and Roger Denlinger[3]

Corresponding author: Jacqueline T. Salzer, Deutsches GeoForschungsZentrum GFZ, Telegrafenberg, Potsdam, Germany. (salzer@gfz-potsdam.de)

[1]Department 2: Physics of the Earth, GFZ German Research Centre for Geosciences, Potsdam, Germany.

[2]Hawaiian Volcano Observatory, U.S. Geological Survey, Hawaii National Park, Hawaii, USA

[3]Cascades Volcano Observatory, U.S. Geological Survey, Vancouver, WA, United States USA.

[4]Univ Lancaster, Lancaster Environment Centre, Lancaster LA1 4YQ, England

Abstract.

Morphological changes and intermittent destabilization of volcanic lava domes can lead to the development of rockfalls and pyroclastic flows, significant ~~components of the~~ volcanic hazards. We study short term dome deformation associated with earthquakes and tremor at Mount St. Helens, recorded by a permanent optical camera and seismic monitoring network. We use Digital Image Correlation (DIC) to compute the displacement field between successive optical images, and compare the results to the occurrence and characteristics of seismic events during a 6-week period of dome growth in 2006. The results reveal that upward dome growth at Mount St. Helens was repeatedly interrupted by short term meter-scale downward displacements at the dome surface. The displacements were associated in time with low frequency, large magnitude seismic events followed by a tremor-like signal. The tremor was only recorded by the seismic stations closest to the dome. We find a correlation between the magnitudes of the camera-derived displacements and the spectral amplitudes of the associated tremor. We derive the 3D-displacements for a representative seismic event by reprojection of the DIC results from two cameras onto the topography, revealing a segmentation of the dome into areas of distinctive displacements. We conjecture that the tremor is recording the gravity-driven response of the upper parts of the dome due to depressurization, mechanical disintegration, and superimposed slumping, controlled by clearly defined internal dome structures. ~~associated with the leading earthquake. Our approach allows the reconstruction of the internal dome architecture and~~

~~identification of structures that control dome deformation.~~ The distribution of such features may have significant implications ~~of~~ for the structural integrity of the dome and the potential for ~~of~~ for collapse. Our results highlight the potential of new techniques, which can also be applied to existing datasets, for revealing details of the dome growth process and the relationships between shallowseismic and deformation signals.

1. Introduction

1.1. Overview

Andesitic and dacitic lava domes are viscous bodies of lava extruded in the summit region or the flank of a volcano over periods of days to decades. Structural instabilities and resulting collapses can lead to far-reaching debris avalanches and pyroclastic flows [*Voight*, 2000], and pose a significant hazard for the surrounding population.

The internal structure of a lava dome has a strong impact on dome stability. In particular the development of shear bands and their propagation into the dome is a key process governing transitions between endogenous and exogenous styles of dome growth [*Hale and Wadge*, 2008]. Substantial morphological and structural changes may also be strongly dependent on the parameters governing the eruption, such as variations in the supply rate and magma rheology [*Husain et al.*, 2014].

Deformation monitoring at dome-building volcanoes may allow resolving the presence of long term internal dome structures [*Beauducel et al.*, 2006; *James and Varley*, 2012] which are critical for numerical modeling [*Hale et al.*, 2009]. However, these signals are mixed with many other processes associated with dome growth that may lead to deformation over a wide range of temporal and spatial scales. E. g., internal pressurization of the lava dome may have large effects on the development of an eruption [*Sparks*, 1997], but may also lead to deformation due to the repeated sealing of gas pathways on time scales of minutes [*Johnson et al.*, 2014] to days or weeks [*Ichihara et al.*, 2013; *Matthews et al.*, 1997]. Experimental data shows that densification may also be driven by viscous reorganization of pores by surface tension on time scales of hours to years [*Kennedy et al.*, 2016].

Data sampling at high temporal resolution has also revealed possible links between seismic signals and mass movement at volcanic domes, e. g. related to inflation-deflation cycles produced by repeated conduit pressurization at Montserrat [*Voight et al.*, 1999]. Long-Period events at the Santiaguito dome can be attributed in time and magnitude to brittle failure of the carapace due to degassing events [*Johnson et al.*, 2008]. A connection between thermal exhalations and dome surface displacements has also been observed at the dome of Volcan de Colima, while extruding over the crater rim [*Walter et al.*, 2013]. Combining the analysis of seismic and deformation data is therefore essential for improving our understanding of the processes controlling them. However, quantifying deformation at volcanic domes and comparison between different events over longer time spans is often challenging due to difficult access, the lack of continuously operating systems and the small magnitude of the deformation. In this work we analyze an existing dataset using novel techniques in order to evaluate dome deformation associated with earthquakes at Mount St. Helens.

1.2. The 2004 - 2008 eruption of MSH

During the 2004 - 2008 dome building eruption of Mount St. Helens, extrusion of a series of andesitic-dacitic spines as well as endogenous growth constructed a dome complex at the base of the crater floor, South of the pre-existing dome from the 1980s [*Vallance et al.*, 2008]. An optical camera monitoring system was installed on the surrounding crater rim by the USGS Cascades Volcano Observatory (CVO), allowing the observation of the growing dome from multiple perspectives. The collected dataset has successfully been used to determine variations in the extrusion rate and evaluate the morphological evolution of the dome complex throughout the eruption [*Major et al.*, 2008, 2009]. The internal dome structure was marked by discontinuities created by spine formation, and also by faulting at the conduit margin and within the spines ~~related to faulting at the conduit margin and spine formation as well as within the spines~~ [*Cashman et al.*, 2008].

On time scales of months to years, the extrusion rate at Mount St. Helens showed a quasi-exponential decrease over the course of the eruption [*Mastin et al.*, 2009; *Diefenbach et al.*, 2012] before ceasing in January 2008 [*Dzurisin et al.*, 2015]. Previous studies revealed variations in the extrusion velocities observed at the dome over sequences of daily images [*Walter*, 2011]. However, the mechanism behind these fluctuations and their relationship to seismic data remains to be studied.

Over prolonged periods, the seismic data were marked by shallow, often regular and repetitive small long period (LP) earthquakes, also named "drumbeats" due to their repetitive behaviour. Occasionally, larger $M > 2$ earthquakes were also recorded, as well as higher frequency volcano-tectonic (VT) earthquakes and volcanic tremor [*Moran et al.*, 2008b; *Thelen et al.*, 2008].

The larger events and the drumbeats shared some similarities in source depth, seismic frequencies and the characteristics of the associated infrasound signals [*Matoza et al.*, 2009; *Moran et al.*, 2008b]. This may suggest a common source mechanism for the smaller LP earthquakes and the larger events, with the main difference being only the event magnitude. Thus, the models proposed for the generation of the drumbeat seismicity have also been applied to the larger earthquakes at Mount St. Helens [*Kendrick et al.*, 2012; *Waite et al.*, 2008].

The mechanisms that have been suggested as possible sources for the drumbeat seismicity and the larger earthquakes at Mount St. Helens fall into two main categories [*Chouet* *and Matoza*, 2013]. On one hand, brittle fracture and stick-slip behavior controlled by friction at the conduit wall [*Iverson et al.*, 2006; *Kendrick et al.*, 2012, 2014], on the other hand, interactions with the hydrothermal system, resulting in the repeated sealing and pressurization of a steam filled crack beneath the crater floor [*Waite et al.*, 2008; *Matoza et al.*, 2009, 2015].

The possible association of seismicity with stick-slip and episodic changes in the extrusion behaviour of the plug as suggested by *Iverson et al.* [2006] led to various attempts to measure short-term deformation at Mount St. Helens, including the installation of a tiltmeter network [*Anderson et al.*, 2010] and a high resolution camera aimed at capturing exclusively the motion of features on the exhumed conduit fault. Deformation associated with the "drumbeat" earthquakes could not be identified, however, some of the larger events showed permanent offsets in the tiltmeters [*Anderson et al.*, 2010].

1.3. Seismicity and deformation at MSH

Here we systematically analyze optical camera data from Mount St. Helens collected over a six-week period in the summer of 2006. We use modern image correlation techniques and a new approach that allows the extraction of 3D displacements from multiple camera perspectives, based on reprojecting pixel displacement data and a high resolution Digital Elevation Model (DEM) [*James et al.*, 2006]. This study focuses on the identification and quantification of short-term pixel displacements and the seismicity, exploring their relationship in time and magnitude. We integrate data from multiple cameras into a common reference frame and systematically compare high-resolution measurements of displacements to seismic data. Our results provide new insights into the internal mechanics of dome growth at Mount St. Helens and the origin of the processes underlying the seismic signals.

2. Data

2.1. Seismic Network

The seismic data used in this study were collected by the University of Washington Pacific Northwest Seismic Network and the USGS Cascades Volcano Observatory. We use predominantly the stations RAFT and SEP, accelerometers located close to the dome, as well as the short-period seismic station HSR located at a distance of 3 km (Figure 1). Data from the short-period seismometers SEP, SHW and JUN, the accelerometer NED and the broadband station STD were also considered. The accelerometers and short period seismometers had a sample rate of 100Hz, while STD was sampled at 50Hz and has a sensitivity down to 60s.

2.2. Camera network

The images used in this study were acquired by Olympus C30-30 digital cameras installed by the USGS Cascades Volcano Observatory (CVO) as part of the remote camera monitoring system [*Poland et al.*, 2008; *Major et al.*, 2008, 2009]. The perspectives on the dome the three cameras offer are shown in Figure 1. The Brutus and Sugarbowl cameras viewed the dome from similar directions, while South Rim was installed on the opposite side of the dome. The different viewing directions of the cameras allows a relatively complete coverage of the dome, comparisons between observations, and a detailed record of observed pixel displacements for linking to seismicity.

The temporal resolution of our deformation measurements is dependent on the frequency of the image acquisitions. At Mount St. Helens, the cameras were acquiring images at regular intervals ranging from every 15 minutes to 1 hour, depending on the camera setup. Additionally, the temporal resolution of our measurements is affected by visibility and time of the day, since images where the dome is obscured by clouds or strongly overexposed have to be discarded. Naturally, images taken during the night cannot be used.

The spatial resolution of our deformation measurements is dependent on the pixel size reprojected on the dome surface, which varies with the camera setup (zoom, image resolution), distance and orientation to the target. The images used here had a resolution of 1280 960 pixels. For pixels projected onto an orthogonal surface, the footprints were calculated to be around 70 cm for Sugarbowl and 35 cm for Brutus using calibration targets captured at close range [*Major et al.*, 2009]. No such calibration is available for the South Rim camera. Considering the sensor specifications, distance to the dome, focal length and image resolution we calculate an approximate pixel footprint of 38 cm. ~~South Rim is positioned at the closest distance to the dome, and with the dome covering the greatest proportion of the image when compared to Brutus and Sugarbowl, therefore having a smaller pixel footprint and the highest resolution on the dome surface.~~

The cameras were set to a higher resolution (2048 x 1536 pixel) towards the end of July. From the events included in the systematic study (see Table 1), only two (Event No. 41, 42) were acquired with the higher resolution. For consistency, they were downsampled prior to the DIC analysis.

3. Methods

3.1. Digital Image Correlation (DIC)

DIC is a computational method used to calculate the 2D displacement field between two successive images [*Pan et al.*, 2009] In the case presented here, the method relies on naturally occurring intensity patterns visible on the rough surface of the dome. The images are first converted to a 2-D matrix of intensity values and coregistered at subpixel level using a reference area outside the deforming area (e.g. on the crater wall or the 1980s dome). The images are then divided into a grid of discretized overlapping sub-regions (see Section 3.2). For each sub-region, the displacements relative to the reference image are calculated by optimizing a Fast Fourier Transform based cross correlation function. We use the StrainMaster package developed by LaVision, which allows for multiple sequential passes with decreasing window sizes and varying amounts of overlap, which iteratively improves the displacement calculations for each sub-region. Erroneous displacement vectors are removed based on their low correlation values as well as median filtering [*Westerweel*, 1994]. Under ideal conditions, DIC can allow displacement calculations with an accuracy of a fraction of a pixel [*Pan et al.*, 2009].

~~The technique is based on the automatic identification of the same textural pattern in sub-regions of successive images by maximizing a correlation coefficient (Pan et al. 2009). The images are first coregistered at subpixel level using a reference area outside the deforming region. The displacement field is then extracted by dividing the images into overlapping sub-regions, for which the correlation function is calculated (Walter, 2011).We use the StrainMaster package developed by LaVision, which allows for varying sub correlation window sizes, amounts of overlap, and multiple passes as well as quality~~

~~control of the resulting displacement vectors. Under ideal conditions, DIC can allow displacement calculations with an accuracy of a fraction of a pixel (Pan et al. 2009)~~.

DIC has become a common remote sensing tool for measuring deformation using terrestrial optical camera systems in a wide range of settings, including volcanoes [*James et al.*, 2007; *Johnson et al.*, 2008; *Walter*, 2011], landslides [*Travelletti et al.*, 2012], and glaciers [*Rosenau et al.*, 2013; *James et al.*, 2015], taking advantage of the low cost, easy hardware installation, as well as its flexibility concerning temporal and spatial resolution. In particular, DIC offers ~~Especially~~ the possibility of measuring displacements at variable time resolutions, covering both the slower and regular displacements as well as short term deformation as expected during an earthquake, which makes it a good tool to study deformation at volcanic domes.

3.2. Database compilation

Due to the overall good weather and availability of data from multiple cameras we chose a period between the end of June and end of July 2006 for this study. During this time period, earthquakes consisted of two types: small amplitude earthquakes occurring at rates of two or more per minute, and larger amplitude earthquakes (M $>$ 2) that occur approximately 3 to 4 times per day. The earthquakes of interest were initially identified based on a threshold of 150 counts ($\sim$11μm/s, assuming a flat response) in the HSR records, which adequately distinguished the larger earthquakes from the smaller "drumbeat" earthquakes. HSR was used, despite being at a distance of 3 km to the dome, since it was easy to identify the stronger earthquakes above the background noise of that station, while the stations close to the dome contained many types of seismic signals associated with dome growth (i.e. rockfalls, drumbeat earthquakes, etc.). Apart from a few exceptions (e.g Event No. 13 or 31 in Table 1), most of the events we identify can also be found in the Pacific Northwest Seismic Network catalogue.

Out of the list of picked events, only those occurring during daylight (approximately 11:30am to 04:30am(+1) UTC) were considered. The image database was then explored to identify those events where data are available from the South Rim and Brutus cameras, since these offered the highest resolution on the dome surface. The images bracketing the seismic event were then analyzed using DIC. The size of the correlation windows used in the DIC varied between 12 and 24 pixels, depending on the amplitude of the pixel displacements to maximize the quality of the DIC result Adjacent widows overlapped by 75%, yielding pixel displacement maps of up to 320 by 427 pixel.

An event was considered to show no displacements only when images from both the SouthRim and Brutus cameras were available, and the DIC results from both cameras showed no displacements. In order for an event to qualify as showing deformation, a clear signal from one camera would suffice (Figure 3).

The clarity of the DIC-derived displacement fields varies between image pairs. Three types of noise may be observed in the DIC results: random noise (the displacement vectors being randomly oriented), spatially correlated noise (identical displacements of neighboring pixels over a larger area) and correlation failing due to changes in the surface pattern (i.e. detachment of material by rockfalls, or an internal reorganization of the clasts). When the correlation is poor, the displacement vectors corresponding to those areas of the image do not pass the sequential quality control in the processing software where we discard vectors with low correlation values or large deviation from their neighbours. Therefore no displacements can be extracted in those parts of the image.

The amount of random and spatially correlated noise depends mainly on the light conditions, the amount of time elapsed between the images, and may also occur if an image is disturbed by haze. Furthermore, images acquired at different lens apertures may lead to apparent pixel displacements due to lens distortions. We minimize this noise by using image pairs which are optically consistent. In some cases this requires skipping one image in the acquisition sequence, therefore increasing the temporal baseline between the images to be correlated. However, in order to restrict the contribution of the regular dome extrusion to the pixel displacements related to the earthquakes, we only allow for a maximum interval of two hours between images.

In general, displacements below 0.4 pixel are discarded as noise, which roughly corresponds to the mean 2-hour pixel displacements we derived from daily images. Image pairs with high levels of noise (correlated, random and due to low correlation) were discarded as inconclusive. Overall, 50-60% of the initially picked seismic events occurring between June 25 and July 11 were excluded from further analysis.

3.3. Calculation of mean pixel displacement and spectral amplitudes

Following the above routine we compiled a catalogue of events which were either clearly associated or not associated with detected pixel displacements (Table 1). For the events associated with displacements, a polygon mask was applied manually to the displacement fields to enclose the area affected by displacements, excluding the sky and other areas lying in the background. From within the polygon, all vectors with magnitudes smaller than the noise threshold were removed. The remaining vectors were then used to calculate the average pixel displacement amplitude and the pixel area affected by displacements.

Subsequently, we analyzed the seismic records of the events associated with displacements for their power spectra and mean spectral amplitudes as a measure for seismic energy release. When the high amplitude earthquake is followed by tremor, we may separate the leading earthquake from the tremor by considering different spectral bands. For the leading earthquake, peak frequencies were between 1 and 5 Hz and thus we calculated the mean of the amplitude of the fast fourier transform within that band. Similarly, the energy of the tremor was localized between 5 and 20 Hz, and we used that range to calculate the mean spectral amplitude of the tremor. This analysis was performed for the statios SEP and RAFT, however, the data from RAFT were most complete during the time period of our study and thus preferred for comparison with mean pixel displacements.

~~Subsequently, we analyzed the seismic data of the events in the previously compiled catalogue in terms of spectral amplitudes. Seismic records from both SEP and RAFT were analyzed for their power spectra and mean spectral amplitude. However, the data from RAFT were most complete during the time period of our study and thus preferred when comparing earthquakes together.~~ ~~In cases where the leading earthquake was followed by tremor, the data were divided and the spectra of the leading earthquake and subsequent tremor were considered individually. For the leading earthquake, peak frequencies were between 1 and 5 Hz and thus we used that window for calculation of the mean spectral amplitude~~.

3.4. Calculation of 3D displacements

The fixed cameras record a two-dimensional and unidirectional field of view. When the target is viewed from similar perspectives, a stereo matching approach can be applied to enable ~~translate~~ the DIC-derived displacement fields to be converted from image space (pixels) into a real 3D space. However, this can rarely be done in natural settings, since suitable locations for camera installations which enable efficient stereo matching are rare. Also, larger viewing angles between cameras are generally preferred to enhance coverage, whereas smaller angles are needed for stereo matching. ~~since the principal goal of volcano observatories is monitoring the activity, larger angles between the cameras, which enhance coverage, are generally preferred, making a stereo matching approach challenging~~ Despite the Sugarbowl and Brutus cameras covering similar areas of the dome, the angle between them is still too large to extract full 3D displacement fields using a stereo-matching DIC approach. Manual identification of individual features on the dome can enable some 3D deformation to be extracted from in multiple camera images [*Major et al.*, 2009], but this sacrifices the high spatial resolution DIC offers.

Instead, we develop a new technique that allows 3D deformation maps to be determined from DIC analyses of multiple cameras when stereo-matching fails. The approach is based on reprojection to a high quality DEM [*James et al.*, 2015], and results in 3D displacements calculated for those areas of the DEM which are covered by the DIC-derived displacement fields from two (or more) cameras. First, the orientation of both cameras is determined by aligning them to the DEM. To identify the areas on the dome which are visible from both the Sugarbowl and Brutus cameras, we reproject the image points representing each Sugarbowl camera pixel onto the triangulated DEM, to derive their 3D coordinates. Any of these 3D points that are not visible in the Brutus camera are then discarded. For the remaining points, their equivalent displaced image positions are determined from the DIC results for both cameras, and are then reprojected. This results in two rays for each displaced point, so that displaced 3D coordinates can be derived by ray intersection.Thus, the displaced 3D point coordinates are not derived directly by reprojecting onto the DEM surface. 3D displacement vectors are determined by the difference between the original 3D points and their displaced equivalents.

Due to the rapidly changing topography at the Mount St. Helens dome, we can only calculate reliable 3D maps for events that occurred close to the time when a DEM was acquired For other times, the unknown relevance of the DEM to the actual dome surface at the time would result in unknown and systematic error in the reprojection and intersction calculations. The DEM acquisition that is closest to the period studied was on August 18, 2006 [*Messerich et al.*, 2008]. A significant seismic event associated with deformation of the dome occured the following day, making it an ideal candidate for the 3D displacement calculation.

3.5. DIC time series

In order to detect any rapid changes occurring on the dome in the absence of a seismic signal, we perform a DIC analysis of the camera data independently of our seismic catalogue. We processed all the July 2006 data from the Brutus and South Rim cameras at 30 minute to one-hour image intervals using DIC, and visually inspected the pixel displacement fields for short-term deformation on the dome. We note that this analysis is incomplete, since the image sequence was interrupted by periods of no visibility. However, several hundred hours of useful camera imagery were examined.

4. Results

Our analysis revealed the repeated occurrence of pixel displacements in the camera imagery related to the seismic events in our catalogue. Out of the 42 seismic events included in this study, 25 were found to be associated with measurable displacements on the dome (Table 1). Based on the DIC time series, we did not detect any short-term pixel displacements on the dome in the absence of seismic shaking.

We will first describe the differences in the seismic records between the events associated with displacements and those that were not. We then describe the DIC results of the co-seismic displacements in detail, and the relationships between the seismic and deformation signals. Finally, we will present the results of the 3D calculations for the event on August 19, 2006.

4.1. Seismicity: differences between events

The analysis of the seismic data showed strong differences between the events associated with pixel displacements and those that were not:

4.1.1. Power Spectral Densities (PSD)

The PSD over the first 20 seconds of events showing displacements had a lower frequency signature when directly compared to events without displacements at the same seismic station (Figure 4). The differences appear stronger in the data from station HSR (Fig. 4A) than SEP (Fig. 4B). This may be due to the greater distance of the station HSR to the dome, and the stronger attenuation of the higher frequencies with greater distance. At HSR, the events associated with pixel displacements show strong components around 1 Hz, similar to the Low Frequency events described in *Horton et al.* [2008] and *Moran et al.* [2008b].

The seismic signals of events that did not show any displacements in the camera imagery (Plotted in brown in Figure 4A/B) had higher frequency signatures, lacking the peak at around 1 Hz, and were more similar to the tectonic events described in *Horton et al.* [2008].

4.1.2. Occurrence of tremor

The events showing pixel displacements in the camera imagery were all followed by a prominent broadband tremor-like signal (Figure 5), with the tremor starting between 10 and 40 seconds after the onset of the main event. Many of these events also had relatively large amplitudes, although several very small events were also associated with pixel displacements (e.g. Event No. 11 and No. 13 in Table 1). The tremor itself is high frequency and only visible in the seismic records from stations located in immediate proximity to the dome (Figure 7), suggesting a surface source with poor seismic coupling, such as a slumping or a rockfall. The duration of the tremor ranges from around one minute to several minutes long. In some cases, events lacking displacements were also followed by tremor (Fig. 6), however it was considerably weaker than the tremor during the events with displacements.

4.2. DIC results

Figure 5 shows the pixel displacement fields from the Brutus and South Rim cameras for two events (Event No. 9 and No. 11). The background colors show the amplitude of the displacement vectors in pixels, the arrows show the direction of the displacements in the plane of the camera view.

The displacements on the dome are clearly visible from both camera perspectives. Their amplitude generally increases towards the center of the area affected by the displacements, reaching maximum amplitudes which exceed 1.5 pixels. Due to the smaller pixel footprint, the displacements observed from South Rim are generally larger than those observed from

Brutus. During Event No. 9, the area affected by displacements in the Brutus camera is approximately 80 m across, with displacement amplitudes of around 40 cm, however, an appropriate conversion from pixels to meters and resolving the full 3D displacement field is only possible applying our new method (Section 4.4).

The DIC displacement fields show two distinguishable areas of differential motion of the dome. One area is located around the top of the dome, well visible from South Rim, but often also from Brutus. Pixel displacements in the central areas of the dome are observed in both events in Figure 5.

The second area is located laterally, towards the right side of the Brutus images (North), involving more of the talus apron. This area is not visible from the South Rim camera and appears as a triangular surface in the Brutus displacement fields. The first event in Figure 5 also shows displacements in this region. Most of the events we analyze in this study show displacements in the central region of the dome, only five involve this lateral (”L”) region. These were highlighted in pink in Table 1. During some events (e. g. Event No. 9 and No. 37), both the central dome and the lateral area would show displacements. Other events would only be associated with displacements in the L region, but not in the central dome (e. g. Events No. 6 and No. 26).

We note that all the displacements we observed occurred within the dome in the area behind the exposed edge of the dome that represented the exhumed conduit fault (visible as the smooth or striated surface in the images). None of the events presented here showed any pixel displacements on the smooth surface of the fault.

The displacement fields of events lacking displacements only involved uncorrelated noise, usually below the the level of 0.4 pixel (Figure 6). No measurable and coherent displacements on the dome were observed to be associated with any of the higher frequency events - even the larger amplitude events or events followed by tremor. However, all LF events for which suitable images were available were associated with displacements.

4.3. Spectral Amplitude Relationships

We calculate the mean spectral amplitudes of the leading earthquake and the tremor and the mean displacements in the Brutus and South Rim cameras following the method described in Section 3.3 in order to evaluate possible links between the causative processes.

4.3.1. Earthquake and Tremor Spectral amplitudes

We observe no clear relationship between the average spectral amplitudes of the leading earthquake and the average spectral amplitude of the subsequent tremor (Fig. 8). Using the camera data, we can distinguish between events which only show displacements in the central dome region (plotted in blue) and those involving displacements in the L region (plotted in red). We note that two largest earthquakes analyzed in this study (Events No. 37 and No. 42) were associated with displacements in the L region. However, they were not associated with particularly strong tremor (red outliers in Fig. 8). Also, relatively small leading earthquakes may be associated with very strong tremor if the displacements occur only in the central area of the dome (blue outliers in Figure 8).

We interpret this result as the generation of the tremor being mechanically different, depending on which area of the dome is affected by the displacements. The 3D calculations (Section 4.4) show that displacements in the L region have an overall smaller vertical component when compared to the central areas of the dome. Events affecting the central region of the dome show a wider range of tremor amplitudes, including high amplitude tremor. Differences in the efficiency at generating high amplitude tremor may be due to a shallower dip on an underlying fault plane, or due to temperature-dependent rheological differences resulting from the larger distance of the L region to the hot dome core. Due to the different ~~mechanics~~behaviour behind the tremor generation in the L region and the central regions, we only consider events with displacements occurring exclusively in the central dome area for the comparison between spectral amplitudes and displacements derived from camera data.

4.3.2. Mean displacements and Spectral amplitudes

We compare the mean displacements visible in the South Rim and Brutus cameras to the average spectral values of the leading earthquakes and the subsequent tremors for each event (Fig. 9). This analysis reveals an apparently linear relationship between the mean pixel displacement magnitude at the South Rim camera and the mean tremor spectral amplitudes. The R-square values for a linear fit (plotted in red in (Fig. 9) are considerably lower for the Brutus camera, possibly reflecting a lower signal to noise ratio due to the reduced spatial resolution, which particularly affects the results from smaller events occurring in the central ~~spine~~ dome.

The loose relationship between the amplitudes of the leading earthquake and the tremor (Fig. 8) leads to similarities in the patterns when plotting either the leading earthquake or tremor spectral amplitudes against the displacements. However, in all cases, the scatter is reduced and the R-square values increased when comparing the displacements against the tremor amplitudes (right column) rather than the earthquake amplitudes (left column), suggesting a closer link between the tremor and the displacements.

In the framework of this study we have also calculated the area of pixels affected by displacements, as well as the "Area integrated displacement", by multiplying the pixel area by the mean displacement. However, we found no correlation between these measurements and the spectral amplitudes of the seismic signals.

4.4. Results of 3D calculations

We use an accurate DEM and the displacement fields calculated by DIC from two cameras to extract a full 3D deformation field for an earthquake that occurred on Aug. 19, the day following the acquisition of the DEM. Due to the need for an accurate DEM and the rapidly changing topography on the crater floor, we could only perform the 3D calculation for this particular event. ~~this could only be done for this event~~

Figure 10A shows the details of the seismic signals and the single camera displacement fields calculated for this event. The spectrogram is similar to those in Figure 5, albeit the event used in the 3D calculation was ~~being~~ of larger magnitude. The higher resolution setting of the cameras at the end of July also contributes to the large amplitude of the pixel displacements seen in the Brutus displacement field in Figure 10A when comparing it to those in Figure 5.

The results of the 3D displacement calculation in a very close-up view of the dome are shown in perspective view (Fig. 10B) and plan view (Fig. 10C). The results cover the section of the dome that is visible from both the Sugarbowl and Brutus cameras. Since the perspective of the South Rim camera is not covered by the other cameras, it could not be used for the 3D displacement calculation. For a larger field of view and orientations of the cameras relative to the dome refer to Figure 1.

The displacements during the Aug. 19 event affected a large surface area of the dome. The diameter of the area of the dome that experiences vertical (downward) displacements greater than of 40 cm exceeds 150 m. The Western limit to the deforming area cannot be constrained due to lack of coverage by both the Brutus and Sugarbowl cameras.

The results of the 3D analysis highlight the segmented fashion of the dome deformation during the earthquakes described in the previous section, and allow estimation of the 3D co-seismic deformation field in very high detail. The displacements within the lateral area previously identified in the Brutus imagery ($\underline{L}$ region) are characterized by displacements towards the North reaching amplitudes of around 40 cm, and vertical displacements of similar amplitudes. These displacements are clearly distinguished from the two areas to the South. The Southeastern region (C_{Br}) displays very large vertical displacements of over one metre, as well as horizontal displacements towards the NE of amplitudes in the range between 50 and 90 cm. The Southwestern area (C_{SR}) displays mainly vertical displacements of around 40 cm, but no horizontal motion.

Within the regions, the magnitude of the vertical displacements as well as the azimuth of the horizontal displacements are almost uniform. The boundary between C_{Br} and C_{SR} is very sharp and we observe a sudden change of the observed horizontal and vertical surface displacements. The transition between the regions C_{SR} and $\underline{L}$ is marked by a narrow, East-West oriented feature where neither horizontal nor vertical displacements are visible the dome surface (Figure 10C).

——————————— ... ———————————

The remaining parts of the paper have been rephrased and restructured significantly. For the sake of readability we refrain from marking the changes

——————————— ... ———————————

5. Discussion

Our results reveal that the steady dome growth at Mount St. Helens was repeatedly interrupted by downwards displacements of the dome reaching magnitudes on the ~~of~~ order of a meter over a time scale of minutes. These were consistently linked to seismic events. Measurable short term pixel displacements were observed exclusively in combination with the occurrence of low frequency earthquakes followed by high frequency tremor. No short term displacements were detected in the absence of such a seismic event, and all lower frequency seismic events in our database for which imagery is available from both the South Rim and Brutus cameras show pixel displacements as well as tremor. While some of higher frequency seismic events are also associated with tremor (e.g. Ref. 2, 8, 12, 27) none show displacements, despite some having relatively large seismic amplitudes (e.g. Ref. 2, 10, 15, 30). Therefore, our results strongly point towards the generation of the leading low frequency earthquake, tremor and dome displacements being linked by a common, repeatable mechanism.

We observe differential motion and strong segmentation into regions or "blocks" limited by narrow, well defined boundaries suggesting the shallow deformation is fault-controlled. The areas in which displacements are observed are bound by the main conduit faults [*Pallister et al.*, 2013]. Within the deforming area, the segmentation occurs along internal dome structures. Such structures may form at deeper levels for example due to the development of shear bands [*Hale and Wadge*, 2008], internal stresses imposed by an oblique intrusion [*Donnadieu and Merle*, 1998], or slumping and spreading of a soft underlying material [*de Vries et al.*, 2000]. Our results suggest that such internal dome structures at Mount St. Helens were activated during the low frequency earthquakes.

Rockfalls and the formation of dust-and-ash plumes were frequently observed in association with large magnitude earthquakes at Mount St. Helens [*Moran et al.*, 2008a]. The frequency content of the tremor signals described in our study is also consistent with slumping or rockfall-like signals [*Hibert et al.*, 2014], and inspection of the optical data as well as areas of correlation loss in the DIC results show that rockfalls also occurred in some of the events analyzed here, and contributed to the seismic signal. However, due to the striking correlation between the mean displacement amplitudes and the mean spectral amplitudes of the tremor the deformation of the dome appears to be the dominant source. The seismic signals we describe here have not previously been linked to deformation of the dome or the process generating low frequency seismicity at Mount St. Helens.

Prior to discussing processes that may explain our observations, we briefly describe the main limiatations of our work.

5.1. Data and method limitations

5.1.1. Camera sampling frequency and clock offset

The exact rate and timing of the displacements relative to the earthquake or tremor signals can not be resolved, due to the low sampling frequency of the cameras. The presented displacement fields therefore usually cover a period of 20-30 minutes surrounding the earthquake in the South Rim camera and up to 1 hour in the Brutus camera (Table 1). Based on the duration of the tremor, the displacements however occur over a time span of 10s of seconds to minutes.

Additionally, exploring the temporal relationship between the tremor and the displacements is complicated by an offset of the internal clock of the South Rim camera. We could constrain this offset to approximately 13 minutes, i.e. the displacements in the imagery from South Rim appear to be delayed relative to the seismic and other camera data. This can be accounted for by choosing an appropriate "later" image pair for the DIC analysis.

5.1.2. Camera resolution and coverage

While DIC allows extraction of displacements at a much higher resolution than other methods, we are not sensitive to displacements smaller than 0.4 px (approx. 15 cm of displacement along a projected surface orthogonal to the Brutus and South Rim camera views). Also, we lack adequate camera observations from the Western side of the crater (Figure 2).

Despite these limitations, under the working hypothesis that *"Larger amplitude, lower frequency events are associated with displacements, while higher frequency ones are not"*, all our samples fulfil this hypothesis. Lack of coverage and resolution does not appear to be an issue. Also, the "DIC time series" analysis (Section 3.5) did not reveal any short term displacements in combination with a tremor-like signal, but lacking a leading earthquake. However, naturally, we cannot exclude that displacements below the detection threshold occurred.

5.1.3. Considerations for future installations

Future camera monitoring systems could be optimized for the detection and quantification of short term dome deformation. More frequent camera acquisitions could increase the temporal resolution, potentially allowing a better understanding of the dynamics of the deformation process. This may have also enable a larger number of events to be analyzed, in particular around dusk and dawn, by reducing the probability that one of the camera acquisitions is in the dark. A higher temporal sampling would also reduce the more subtle changes in the lighting conditions as well as the contribution of "regular" dome growth to the displacement signal, and therefore the error in displacement calculations. If images are acquired more frequently, the accuracy of the camera clocks becomes increasingly critical to constrain the timing of any displacement and its relationship to other high-rate geophysical datasets. Therefore, synchronization of the cameras with a GPS clock should be considered. Furthermore, a larger number of cameras, with greater overlap in the fields of view, as well as more frequent high resolution DEMs acquired e.g. from drone or helicopter overflights as routinely done nowadays, would allow 3D displacement maps to be constructed for more seismic events.

5.2. Earthquake and deformation processes

In the following section we will discuss processes that may explain our observations. We can group the proposed mechanisms into two kinds:

1. Mechanisms that provide an explanation for both the leading earthquake and the displacements and tremor (”Single-step mechanisms”),

2. Mechanisms that may explain the dome displacements and the time scale over which they occur, but do not have the capacity for accumulating the the strain needed to generate the leading earthquake. In these cases, we require a separate (independent) mechanism for the leading earthquake, and the observed displacements and tremor are related to the response of the dome to the passing seismic waves (”Triggered mechanisms”).

5.2.1. Single-step mechanisms

Plug Stick-Slip

Previous works have proposed two possible source processes for the low frequency seismicity at Mount St. Helens On one hand, friction between the ascending plug and the conduit margin leads to the build-up of stress, which is released by shear failure during an upwards "slip" of the plug during the earthquake [*Iverson et al.*, 2006; *Kendrick et al.*, 2012, 2014]. *Kendrick et al.* [2012] also applied their model to one of the earthquakes included in this study (Event No. 42 in Table 1). According to their calculations, the co-seismic slip would correspond to upward displacements of the dome in the range of 0.81 to 3.05 m. For motion occurring along a plane orthogonal to the viewing direction of the Brutus camera, this would correspond to 4 to 12 pixels of displacement, which lies well above our detection threshold of 0.4 pixel. However, we do not observe any upwards displacements or large slip on the fault surface during any of the earthquakes. Our observations therefore do not support the *Kendrick et al.* [2012] model. Also, the apparent "stalling" of spine 7 in sequences composed of daily images, mentioned by *Kendrick et al.* [2012], appears to not be a real decrease in the extrusion velocity of parts of the spine, but rather a superposition of the regular (upwards) displacements [*Walter*, 2011] and the co-seismic (downwards) displacements that occur during large earthquakes. However, we note that the process described by *Kendrick et al.* [2012] may be taking place at depth. The magnitude visible at the surface would also be reduced if the plug is not rigid, or fractured between the earthquake source location and the dome surface.

Pessurized Crack collapse

An alternative hypothesis for the LP seismicity at Mount St. Helens involves the repeated collapse, resonance and re-pressurization of a steam filled sub-horizontal crack in the hydrothermal system [*Waite et al.*, 2008; *Matoza and Chouet*, 2010; *Matoza et al.*, 2009]. Source mechanisms and locations were derived for earlier events, occurring in 2005. These were found to be dominated by volumetric moment tensor components and originated from a shallow acquifer in the southern area of the crater [*Waite et al.*, 2008;

Matoza et al., 2015]. A source process composed of a crack buried at shallow depth, and episodically venting into the overlying loosely consolidated material through a network of fractures was found to reconcile the observed seismic and impulsive infrasound signals [*Matoza et al.*, 2009].

We found similarities between events presented in our study and the two larger earthquakes studied in *Waite et al.* [2008]. The events occurring on July 2, 2005 (13:30) and July 30, 2005 (9:34) described by *Waite et al.* [2008] were both associated with tremor recorded only by the stations closest to the dome and included an initial long period phase that closely resembles the spectra of the events we analyzed.

The displacements oberved in our study are however constrained to the central region of the dome. If we apply the model of *Waite et al.* [2008] to the leading long period part of the earthquakes, steam or magmatic gas would slowly accumulate in distinct regions or a network of fractures within the dome, possibly at the discontinuity associated with the crater floor. The low frequency earthquake is generated as the threshold pressure is exceeded and the "crack" or fracture network collapses and degasses through the permeable upper dome. Following the evacuation and pressure drop, the dome pile at the surface collapses gravitationally (Figure 11). The displacements observed in the camera data would reflect the structural adjustment of the fractured and loosely consolidated material above the crack to the new conditions, taking place over the duration of the tremor (10s of seconds to minutes). A sagging response of the dome to the evacution of the crack has already been hypothesized by *Waite et al.* [2008].

Our observations are in general consistent with this model. However, it remains arguable whether the fractured and porous material above the crater floor is capable of retaining a significant volume of gas under pressure. Also, water from a hydrothermal system would have been boiled off relatively early during the eruption. Lastly, in order to provide a repeatable source for the LP seismicity, a pressurized crack or fracture network located within the dome or conduit would have to be continuously re-established, as it would otherwise move upward with the dome material.

Mechanical collapse

One might also consider a third mechanism, where the gravitational collapse is a driving mechanism and may generate both the leading earthquake and the displacements. This hypothesis is based on the gravitational stress and the bending forces acting on the dome as it is being extruded at an angle, rather than vertically [*Vallance et al.*, 2008]. The accumulating load leads to the buildup of stress on internal faults, which is released episodically by and internal break-up of the dome (Figure 12).

The gravitational impact of the overlying dome on the crater floor may also explain the mostly down first motions and volumetric components observed in the seismic data. In contrast to shear fracturing at the conduit margin [*Holland et al.*, 2011; *Kendrick et al.*, 2012], this mechanism involves shear failure within the dome. We can not constrain whether the fault control that we can distinguish from the surface displacements reflect the upwards propagation of the internal shear faults, or rather shallow secondary features. Due to the ongoing extrusion and morphological changes, individual structures may not be long lived, but instead re-develop in optimal orientations based on the current stress field.

5.2.2. Two-step mechanisms

The second class of mechanisms are not capable of generating the leading earthquake, yet, they do have the potential for generating the observed surface displacements. The processes we briefly discuss below may act on temporal scales from 10s of seconds to days, and may occur independently or be triggered when the dome material is agitated by the passing seismic waves of an independently generated earthquake.

Outgassing occurs when steam or gas that has separated from the magma rises and escapes to the surface or dissipates into the surrounding host rock, leading to compaction [*Ichihara et al.*, 2013; *Matthews et al.*, 1997] or fracturing at the conduit margin and degassing [*Holland et al.*, 2011]. While this may generate larger magnitude earthquakes as discribed in Section 5.2.1, it may also occur as a consequence of passing seismic waves triggering decompression and de-pressurization of deeper seated magma below the crater floor level. The gravitational re-adjustment or the dome pile above the conduit by structurally controlled slumping would explain the surface displacements we observe. However, the 2004-2008 Mount St. Helens dome dacite was notably gas poor and degassed at depth [*Pallister et al.*, 2008], with well established degassing pathways along the conduit margin [*Gaunt et al.*, 2014]. Also, the camera data did not systematically show gas or steam plumes in association with surface displacements.

Viscous reorganization of the pores by relaxation of the surface tension may lead to densification while retaining high permeability of the magma. The importance of this process increases with smaller pore scales and may contribute to deformation in particular over time scales of hours to years [*Kennedy et al.*, 2016]. The displacements we observe however take place over 10s of seconds to minutes. Also, the Mount St. Helens magma solidified at a depth of around 1 kilometer below the vent, and above this level, deformation was entirely brittle [*Pallister et al.*, 2008].

The erupted material **thermally contracts** and densifies as it cools. Due to the timing of this study however we would expect a well established thermal aureole around the conduit. Also, during the ongoing eruption the cooling magmatic column is constantly being replaced by new material. We can therefore consider the overall temperature gradients to be stable, and thermal contraction only playing a minor role in the surface displacements.

In response to seismic shaking, **slumping** may occur when the unstable material of the dome pile slides downslope along shallow detachment planes or discontinuities. In general, we may expect a re-accumulation of displaced material at the bottom of the detachment plane, where we would expect a decrease in the vertical and an increase in the horizontal components of the displacement vectors. While we do observe slight changes in the components when going downslope in the L and C_{Br} regions, we can not identify any accumulation or bulging at the bottom. However, due to the thin-skinned nature of the process any accumulation can spread over a large area, and occur outside the camera view. Slumping, controlled by shallow structures, is however a plausible mechanism, in particular considering the large slope-parallel components of the obeserved displacements.

Repacking and gravitational consolidation of the erupted clasts or blocks may be triggered by the leading earthquake, increasing the static stability of the dome pile. This process decouples the time frame during which displacements occur from when the densification of the blocks takes place, i. e. bubble collapse or slow outcassing may operate over hours (or even days) between the earthquakes, but the compaction of the pile as a whole occurs during seconds or minutes following the earthquake. In order for DIC to work, however, it is important that the pattern (and thus the relative orientation of the clasts) is stable between the images. If the clasts rotate individually, the pattern would change, reducing the correlation in that area, and not allowing the calculation of displacements. Our results show that different areas of internally coherent competent rock move in the same direction, the pattern on the surface remaining the same, rather than loss of correlation due to internal reorganization of the clasts.

5.3. Conceptual model

While some of the processes discussed in Section 5.2.2 are tentative and likely to be triggered by seismic shaking, we point out that we do not observe any displacements associated with any of the larger amplitude high frequency earthquakes, which also have strong peak accelerations. If outgassing, viscous pore reorganization or shallow slumping played a significant role, we would also expect them to be triggered by the high frequency events, which is not the case. We recognize that the dome structures may be more sensitive to lower frequency waves that travel along the conduit, producing surface waves and their amplitudes being enhanced [*Neuberg et al.*, 2000]. However, we favour a conceptual model that unifies all our observations.

We believe that our results leave room for various interpretations but propose that structurally controlled desintegration of the upper dome by shallow faulting and slumping, as shown in Figure 12, play a dominant role. Degassing from a steam-filled fracture network at the crater floor level, as suggested in Figure 11, is also plausible, the displacements we observe being the integrated result of the gravitational response. Furthermore, combinations of these mechanisms (e.g. internal faulting opening pathways for gas propagation) also appear intuitive.

5.4. Dome extrusion dynamics

The occurrence of seismic events linked to dome deformation has a strong effect on the measured daily extrusion velocities. We apply the 3D method to calculate the surface displacements over 24 hours. Since the pixel displacements need to be re-projected on the DEM, a good match between the images and the topography can only be obtained for the days surrounding the DEM acquisition on August 18th (Section 3.4).

Figure 13 shows the 3D surface displacements over three time frames. The panel on the left (A) shows 24 hours of "regular" dome extrusion between August 17 and 18, during which no larger magnitude lower frequency events occurred. The displacements are marked by upwards extrusion and translation towards the West and Northwest, with the vertical components in the dome area reaching around half a meter, and horizontal components up to 1.5 m. Sudden gradients in direction and rate of displacements are indicative for partition of motion along internal dome faults.

The second time frame (Figure 13B) also covers 24 hours, but includes the large magnitude seismic event from August 19 described in Section 4.4. The short term displacements during this event are also shown (Panel C, "Coseismic"). The downwards displacements associated with the earthquake compensate for the regular growth in the central spine, and significantly alter the overall displacement field.

Modern methods of volcano monitoring are increasingly providing high-rate observations of deformation at volcanic domes. However, when reaching a temporal resolution on the order of days, the displacements resulting from contributions from structural modifications and gravity-driven deformation may overprint or even dominate over any changes originating from processes such as variations in the injection rate of magmatic material, or in the friction on the conduit faults. Isolating the relative contributions of these processes to measured dome deformation should be considered in future dynamic and kinematic studies and for better constraining experimental and computational models of dome extrusion.

6. Conclusions

Our systematic study of digital camera imagery of dome growth at Mount St. Helens in combination with the seismicity reveals that large magnitude low frequency earthquakes were associated with strong vertical and down-slope displacements of the upper dome material and a tremor-like signal, sometimes over several minutes long. The amplitudes of the tremor strongly correlate with ~~appear to be closely linked to~~ the amplitudes of the observed displacements.

We demonstrate that these displacements occur only in combination with the low frequency earthquakes and the tremor. This points towards a common underlying mechanism producing the three signals. We propose that the deformation we observe reflects the gravity driven response of the dome to stresses imposed by the inclined extrusion or to depressurization.~~We follow the model proposed by previous authors, where depressurization generates the low frequency earthquake In addition, triggered settling of the dome pile may also contribute to the displacements.~~

The tremor-like signal, recording the displacements of the dome, was observed only in the seismic stations closest to the spine. The proximity of the monitoring instruments to the dome is therefore critical for the investigation and correct interpretation of such shallow volcanic signals.

We successfully applied our new method to derive the 3D displacement fields associated with one seismic event and for two 24-hour periods. The results show that the regular upwards dome growth at Mount St. Helens was occasionally offset by co-seismic downwards vertical displacements of the order of a meter, which significantly affected the calculated daily velocities. Our 3D approach also reveals the internal dome structures activated during the events. The existence, location and distribution of structural discontinuities such as the ones found in this study are of high relevance for numerical and experimental modeling, as they strongly influence the stress distribution within the dome and potentially lead to local destabilization and disintegration of the spine. Deformation monitoring at volcanic domes is therefore crucial for the localization of potentially unstable areas and for understanding mechanisms of dome deformation and destabilization.

...

Appendix A: Examples of 24-hour pixel displacements in July

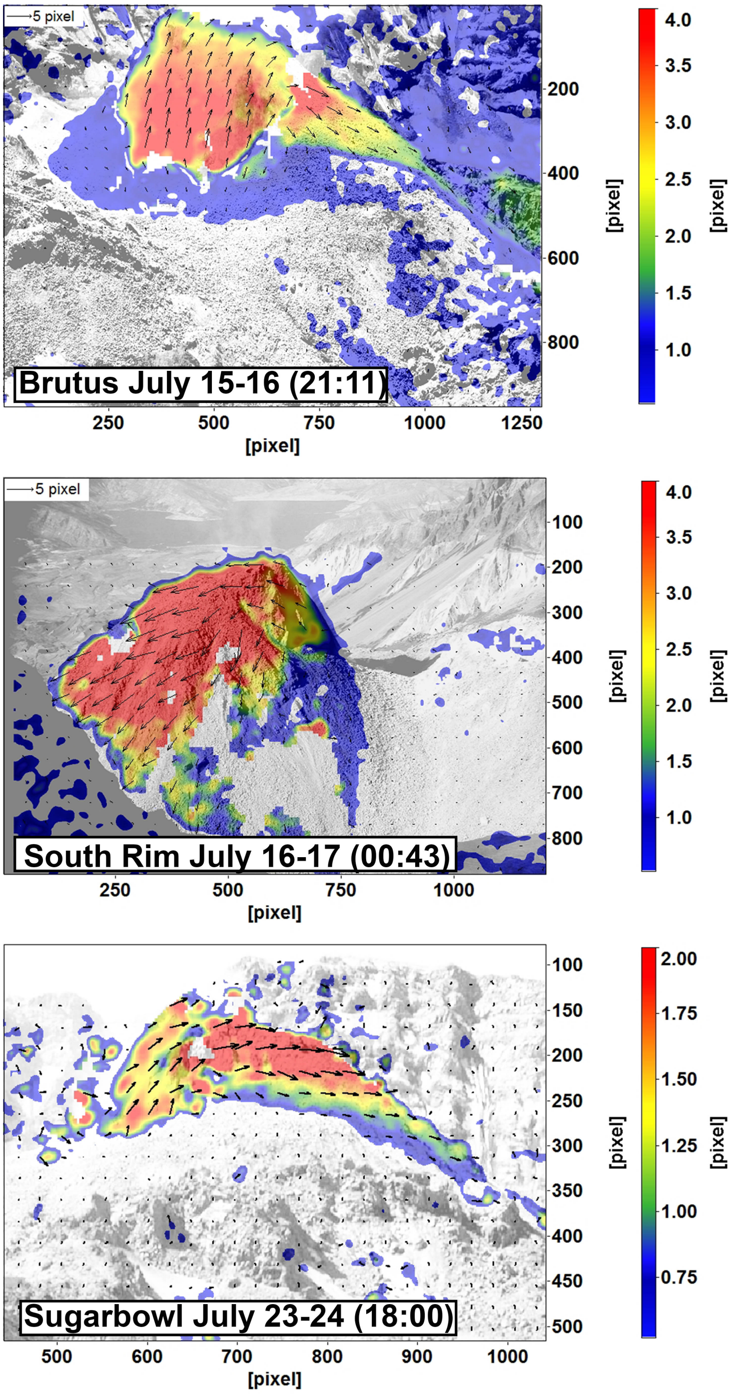

Appendix B: Waveforms used for calculation of PSDs in Figure 4

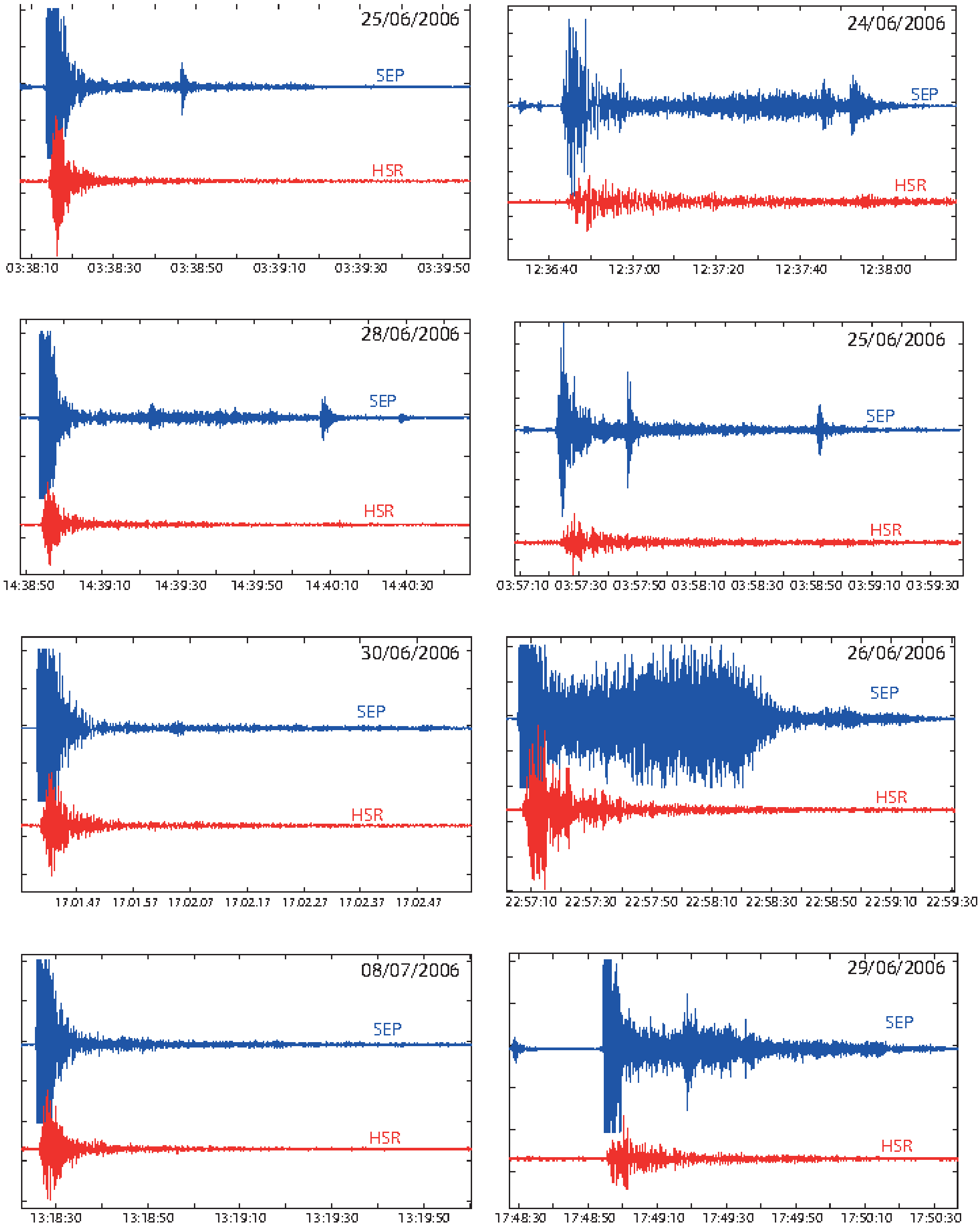

Acknowledgments. This is a contribution to VOLCAPSE, a research project funded by the European Research Council under the European Union's H2020 Programme / ERC consolidator grant n. ERC-CoG 646858. Funding for JS for visiting CVO in July 2014 was provided by the German Academic Exchange Sevice (DAAD). The camera images were provided by the USGS Cascades Volcano Observatory (CVO). The Seismic data was provided by the University of Washington Pacific Northwest Seismic Network and CVO. Figures 8, 9, 10C and 13 were created using GMT [*Wessel et al.*, 2013]

———————————— ... ————————————

References

Anderson, K., M. Lisowski, and P. Segall (2010), Cyclic ground tilt associated with the 2004 -2008 eruption of Mount St. Helens, *Journal of Geophysical Research: Solid Earth*, *115*(B11), B11,201.

Beauducel, F., M. A. Nandaka, F. Cornet, and M. Diament (2006), Mechanical discontinuities monitoring at merapi volcano using kinematic gps, *Journal of volcanology and geothermal research*, *150*(1), 300–312.

Cashman, K. V., C. R. Thornber, and J. S. Pallister (2008), From dome to dust: Shallow crystallization and fragmentation of conduit magma during the 2004-2006 dome extrusion of Mount St. Helens, Washington, *US Geological Survey professional paper*, (1750), 387–413.

Chouet, B. A., and R. S. Matoza (2013), A multi-decadal view of seismic methods for detecting precursors of magma movement and eruption, *Journal of Volcanology and Geothermal Research*, *252*, 108 – 175.

de Vries, B. v. W., N. Kerle, and D. Petley (2000), Sector collapse forming at Casita volcano, Nicaragua, *Geology*, *28*(2), 167–170.

Diefenbach, A. K., J. G. Crider, S. P. Schilling, and D. Dzurisin (2012), Rapid, low-cost photogrammetry to monitor volcanic eruptions: an example from Mount St. Helens, Washington, USA, *Bulletin of volcanology*, *74*(2), 579–587.

Donnadieu, F., and O. Merle (1998), Experiments on the indentation process during cryptodome intrusions: new insights into Mount St. Helens deformation, *Geology*, *26*(1), 79–82.

Dzurisin, D., S. C. Moran, M. Lisowski, S. P. Schilling, K. R. Anderson, and C. Werner (2015), The 2004–2008 dome-building eruption at Mount St. Helens, Washington: epilogue, *Bulletin of Volcanology*, *77*(10), 1–17, doi:10.1007/s00445-015-0973-4.

Gaunt, H. E., P. R. Sammonds, P. G. Meredith, R. Smith, and J. S. Pallister (2014), Pathways for degassing during the lava dome eruption of Mount St. Helens 2004–2008, *Geology*, *42*(11), 947–950.

Hale, A., E. Calder, G. Wadge, S. Loughlin, and G. Ryan (2009), Modelling the lava dome extruded at soufrire hills volcano, montserrat, august 2005may 2006: Part i: Dome shape and internal structure, *Journal of Volcanology and Geothermal Research*, *187*(12), 53 – 68, doi:http://dx.doi.org/10.1016/j.jvolgeores.2009.08.023.

Hale, A. J., and G. Wadge (2008), The transition from endogenous to exogenous growth of lava domes with the development of shear bands, *Journal of Volcanology and Geothermal Research*, *171*(3), 237–257.

Hibert, C., A. Mangeney, G. Grandjean, C. Baillard, D. Rivet, N. M. Shapiro, C. Satriano, A. Maggi, P. Boissier, V. Ferrazzini, and W. Crawford (2014), Automated identification, location, and volume estimation of rockfalls at piton de la fournaise volcano, *Journal of Geophysical Research: Earth Surface*, *119*(5), 1082–1105, doi:10.1002/2013JF002970.

Holland, A. P., I. M. Watson, J. C. Phillips, L. Caricchi, and M. P. Dalton (2011), Degassing processes during lava dome growth: Insights from Santiaguito lava dome, Guatemala, *Journal of Volcanology and Geothermal Research*, *202*(12), 153 – 166, doi: http://dx.doi.org/10.1016/j.jvolgeores.2011.02.004.

Horton, S. P., R. D. Norris, and S. Moran (2008), Broadband characteristics of earthquakes recorded during a dome-building eruption at Mount St. Helens, Washington, between October 2004 and May 2005, *US Geological Survey professional paper*, (1750), 97–110.

Husain, T., D. Elsworth, B. Voight, G. Mattioli, and P. Jansma (2014), Influence of extrusion rate and magma rheology on the growth of lava domes: Insights from particle-dynamics modeling, *Journal of Volcanology and Geothermal Research*, *285*(0), 100–117.

Ichihara, M., J. J. Lyons, and A. Yokoo (2013), Switching from seismic to seismo-acoustic harmonic tremor at a transition of eruptive activity during the Shinmoe-dake 2011 eruption, *Earth, Planets and Space*, *65*(6), 633–643, doi:10.5047/eps.2013.05.003.

Iverson, R. M., D. Dzurisin, C. A. Gardner, T. M. Gerlach, R. G. LaHusen, M. Lisowski, J. J. Major, S. D. Malone, J. A. Messerich, S. C. Moran, et al. (2006), Dynamics of seismogenic volcanic extrusion at Mount St Helens in 2004–05, *Nature*, *444*(7118), 439–443.

James, M., S. Robson, H. Pinkerton, and M. Ball (2006), Oblique photogrammetry with visible and thermal images of active lava flows, *Bulletin of Volcanology*, *69*(1), 105–108.

James, M. R., and N. Varley (2012), Identification of structural controls in an active lava dome with high resolution dems: Volcn de colima, mexico, *Geophysical Research Letters*, *39*(22), n/a–n/a, doi:10.1029/2012GL054245.

James, M. R., H. Pinkerton, and S. Robson (2007), Image-based measurement of flux variation in distal regions of active lava flows, *Geochemistry, Geophysics, Geosystems*, *8*(3), n/a–n/a.

James, M. R., P. How, and P. R. Wynn (2015), Pointcatcher software: analysis of glacial time-lapse photography and integration with multi-temporal digital elevation models, *J. Glaciol.*, doi:10.1017/jog.2016.27.

Johnson, J. B., J. M. Lees, A. Gerst, D. Sahagian, and N. Varley (2008), Long-period earthquakes and co-eruptive dome inflation seen with particle image velocimetry, *Nature*, *456*(7220), 377–381.

Johnson, J. B., J. J. Lyons, B. J. Andrews, and J. M. Lees (2014), Explosive dome eruptions modulated by periodic gas-driven inflation, *Geophysical Research Letters*, *41*(19), 6689–6697, 2014GL061310.

Kendrick, J., Y. Lavallée, T. Hirose, G. Di Toro, A. Hornby, S. De Angelis, and D. Dingwell (2014), Volcanic drumbeat seismicity caused by stick-slip motion and magmatic frictional melting, *Nature Geoscience*, *7*(6), 438–442.

Kendrick, J. E., Y. Lavalle, A. Ferk, D. Perugini, R. Leonhardt, and D. B. Dingwell (2012), Extreme frictional processes in the volcanic conduit of Mount St. Helens (USA) during the 2004-2008 eruption, *Journal of Structural Geology*, *38*(0), 61–76.

Kennedy, B. M., F. B. Wadsworth, J. Vasseur, C. I. Schipper, A. M. Jellinek, F. W. von Aulock, K.-U. Hess, J. K. Russell, Y. Lavalle, A. R. Nichols, and D. B. Dingwell (2016), Surface tension driven processes densify and retain permeability in magma and lava, *Earth and Planetary Science Letters*, *433*, 116 – 124, doi: http://dx.doi.org/10.1016/j.epsl.2015.10.031.

Major, J. J., C. G. Kingsbury, M. P. Poland, and R. G. Lahusen (2008), Extrusion rate of the Mount St. Helens lava dome estimated from terrestrial imagery, November 2004-December 2005, *US Geological Survey professional paper*, (1750), 237–255.

Major, J. J., D. Dzurisin, S. P. Schilling, and M. P. Poland (2009), Monitoring lava-dome growth during the 2004-2008 Mount St. Helens, Washington, eruption using oblique terrestrial photography, *Earth and Planetary Science Letters*, *286*(1–2), 243–254.

Mastin, L. G., M. Lisowski, E. Roeloffs, and N. Beeler (2009), Improved constraints on the estimated size and volatile content of the Mount St. Helens magma system from the 2004-2008 history of dome growth and deformation, *Geophysical Research Letters*, *36*(20), n/a–n/a, doi:10.1029/2009GL039863, l20304.

Matoza, R. S., and B. A. Chouet (2010), Subevents of long-period seismicity: Implications for hydrothermal dynamics during the 2004–2008 eruption of Mount St. Helens, *Journal of Geophysical Research: Solid Earth*, *115*(B12), n/a–n/a.

Matoza, R. S., M. A. Garcs, B. A. Chouet, L. D'Auria, M. A. H. Hedlin, C. De Groot-Hedlin, and G. P. Waite (2009), The source of infrasound associated with long-period events at Mount St. Helens, *Journal of Geophysical Research: Solid Earth*, *114*(B4), B04,305.

Matoza, R. S., B. A. Chouet, P. B. Dawson, P. M. Shearer, M. M. Haney, G. P. Waite, S. C. Moran, and T. D. Mikesell (2015), Source mechanism of small long-period events at Mount St. Helens in July 2005 using template matching, phase-weighted stacking, and full-waveform inversion, *Journal of Geophysical Research: Solid Earth*, pp. n/a–n/a, doi:10.1002/2015JB012279, 2015JB012279.

Matthews, S. J., M. C. Gardeweg, and R. S. J. Sparks (1997), The 1984 to 1996 cyclic activity of lascar volcano, northern chile: cycles of dome growth, dome subsidence, degassing and explosive eruptions, *Bulletin of Volcanology*, *59*(1), 72–82.

Messerich, J. A., S. P. Schilling, and R. A. Thompson (2008), Digital Elevation Models of the pre-eruption 2000 crater and 2004–07 dome-building eruption at Mount St. Helens, Washington, USA, *U.S. Geological Survey Open-File Report 2008–1169, 2p.*

Moran, S., R. Matoza, M. Garcs, M. Hedlin, D. Bowers, W. Scott, D. Sherrod, and J. Vallance (2008a), Seismic and acoustic recordings of an unusually large rockfall at Mount St. Helens, Washington, *Geophysical Research Letters*, *35*(19).

Moran, S. C., S. D. Malone, A. I. Qamar, W. A. Thelen, A. K. Wright, and J. Caplan-Auerbach (2008b), Seismicity associated with renewed dome building at Mount St. Helens, 2004-2005, *US Geological Survey professional paper*, (1750), 27–60.

Neuberg, J., R. Luckett, B. Baptie, and K. Olsen (2000), Models of tremor and low-frequency earthquake swarms on Montserrat, *Journal of Volcanology and Geothermal Research*, *101*(1–2), 83 – 104, doi:http://dx.doi.org/10.1016/S0377-0273(00)00169-4.

Pallister, J. S., C. R. Thornber, K. V. Cashman, M. A. Clynne, H. A. LOWERS, C. W. Mandeville, I. K. Brownfield, and G. P. Meeker (2008), Petrology of the 2004-2006 Mount St. Helens lava dome-implications for magmatic plumbing and eruption triggering, *US Geological Survey professional paper*, (1750), 647–702.

Pallister, J. S., K. V. Cashman, J. T. Hagstrum, N. M. Beeler, S. C. Moran, and R. P. Denlinger (2013), Faulting within the Mount St. Helens conduit and implications for volcanic earthquakes, *Geological Society of America Bulletin*, *125*(3-4), 359–376.

Pan, B., K. Qian, H. Xie, and A. Asundi (2009), Two-dimensional digital image correlation for in-plane displacement and strain measurement: a review, *Measurement Science and Technology*, *20*(6), 062,001.

Poland, M., D. Dzurisin, R. LaHusen, J. Major, D. Lapcewich, E. Endo, D. Gooding, S. Schilling, and C. Janda (2008), Remote camera observations of lava dome growth at Mount St. Helens, Washington, October 2004 to February 2006, *US Geological Survey Professional Paper*, (1750), 225–236, cited By 10.

Rosenau, R., E. Schwalbe, H.-G. Maas, M. Baessler, and R. Dietrich (2013), Grounding line migration and high-resolution calving dynamics of Jakobshavn Isbrae, West Greenland, *Journal of Geophysical Research: Earth Surface*, *118*(2), 382–395, doi: 10.1029/2012JF002515.

Sparks, R. S. J. (1997), Causes and consequences of pressurisation in lava dome eruptions, *Earth and Planetary Science Letters*, *150*(3), 177–189.

Thelen, W. A., R. S. Crosson, and K. C. Creager (2008), Absolute and relative locations of earthquakes at Mount St. Helens, Washington, using continuous data: Implications for magmatic processes, *US Geological Survey professional paper*, (1750), 71–95.

Travelletti, J., C. Delacourt, P. Allemand, J. P. Malet, J. Schmittbuhl, R. Toussaint, and M. Bastard (2012), Correlation of multi-temporal ground-based optical images for landslide monitoring: Application, potential and limitations, *ISPRS Journal of Photogrammetry and Remote Sensing*, *70*(0), 39–55.

Vallance, J. W., D. J. Schneider, and S. P. Schilling (2008), Growth of the 2004-2006 lava-dome complex at Mount St. Helens, Washington, *US Geological Survey professional paper*, (1750), 169–208.

Voight, B. (2000), Structural stability of andesite volcanoes and lava domes, *Philosophical Transactions of the Royal Society of London. Series A: Mathematical, Physical and Engineering Sciences*, *358*(1770), 1663–1703.

Voight, B., R. S. J. Sparks, A. D. Miller, R. C. Stewart, R. P. Hoblitt, A. Clarke, J. Ewart, W. P. Aspinall, B. Baptie, E. S. Calder, P. Cole, T. H. Druitt, C. Hartford, R. A. Herd, P. Jackson, A. M. Lejeune, A. B. Lockhart, S. C. Loughlin, R. Luckett, L. Lynch, G. E. Norton, R. Robertson, I. M. Watson, R. Watts, and S. R. Young (1999), Magma flow instability and cyclic activity at Soufriere Hills Volcano, Montserrat, British West Indies, *Science*, *283*(5405), 1138–1142, doi:10.1126/science.283.5405.1138.

Waite, G. P., B. A. Chouet, and P. B. Dawson (2008), Eruption dynamics at Mount St. Helens imaged from broadband seismic waveforms: Interaction of the shallow magmatic and hydrothermal systems, *Journal of Geophysical Research: Solid Earth*, *113*(B2), B02,305.

Walter, T. R. (2011), Low cost volcano deformation monitoring: optical strain measurement and application to Mount St. Helens data, *Geophysical Journal International*, *186*(2), 699–705.

Walter, T. R., D. Legrand, H. D. Granados, G. Reyes, and R. Armbula (2013), Volcanic eruption monitoring by thermal image correlation: Pixel offsets show episodic dome growth of the Colima volcano, *Journal of Geophysical Research: Solid Earth*, *118*(4), 1408–1419, doi:10.1002/jgrb.50066.

Wessel, P., W. H. F. Smith, R. Scharroo, J. Luis, and F. Wobbe (2013), Generic Mapping Tools: Improved Version Released, *Eos, Transactions American Geophysical Union*, *94*(45), 409–410.

Westerweel, J. (1994), Efficient detection of spurious vectors in particle image velocimetry data, *Experiments in Fluids*, *16*(3), 236–247, doi:10.1007/BF00206543.

Table 1: Table of seismic events and camera data analysed, and results of the spectral amplitude an displacement calculations. See table below for description of acronyms. Note that the internal clock of the South Rim Camera time is approx. 13 min early, the pixel displacements therefore appear to be delayed relative to the seismic event (see Section 5.1.1). Events involving displacements in the L region are highlighted in pink. The lower part of the table contains only events showing displacements, used to make the comparison with the seismic amplitudes more robust.

No.	**Event date**	**Event time**	$\mathbf{SA_{EQ}}$	$\mathbf{SA_{Trem}}$	**South Rim**			**Brutus**		
					im1	im2	D_M [px]	im1	im2	D_M [px]
1	20060624	12:36:50	9.6	7.78	12:44	12:59	1.7	12:24	12:44	–
2	20060625	03:38:10			03:59	04:14	–	03:10	04:10	–
3	20060625	03:57:20	6.57	4.02	03:44	03:59	1.6	03:10	04:10	–
4	20060625	23:58:55	36.9	11.9	23:59	00:29	2.4	23:24	00:11	1.2
5	20060626	04:35:45			04:29	04:59	–	04:24	04:44	–
L6	20060626	22:57:10	26.4	7.82	22:44	23:29	–	22:44	23:04	1.6
7	20060628	03:12:40	20.5	5.9	03:14	03:29	1.6	23:11	04:04	–
8	20060628	14:39:00			14:14	15:14	–	14:24	15:10	–
CL9	20060629	17:48:55	17.2	1.75	17:29	18:44	1.0	17:44	18:04	0.83
10	20060629	19:26:16			18:44	20:14	–	19:10	20:10	–
11	20060629	20:47:19	14.1	4.25	20:14	22:59	1.2	20:10	21:10	0.63
12	20060630	01:32:00			01:29	01:59	–	01:24	01:44	–
13	20060630	12:00:20	4.7	2.49	11:59	12:14	1.1	11:44	12:04	–
14	20060630	17:01:40			16:59	17:29	–	16:44	17:10	–
15	20060701	15:00:45			15:08	15:38	–	14:23	15:10	–
16	20060703	17:26:40			17:08	18:08	–	17:10	18:11	–
17	20060704	00:35:20			00:23	01:08	–	00:10	01:10	–
18	20060704	15:47:39			15:38	16:08	–	15:23	16:10	–
19	20060704	22:32:30	14.6	7.37	22:38	22:53	1.6	22:10	23:10	1.0
20	20060705	02:39:09			02:38	03:08	–	02:10	03:10	–
21	20060705	16:22:50			16:08	16:53	–	16:10	16:43	–
22	20060706	02:36:20	30.8	10.1	02:38	02:53	2.4	02:11	03:10	1.2
23	20060707	16:29:40	17.9	9.53	16:33	16:53	1.7	16:10	17:10	1.0
24	20060707	17:23:10			17:13	17:53	–	17:10	18:04	–
25	20060708	13:18:30			13:13	13:43	–	13:10	13:23	–
L26	20060708	16:47:20	20.1	5.51	16:33	17:23	–	16:10	17:10	2.0
27	20060709	03:02:30			03:02	03:32	–	02:43	03:10	–
28	20060709	12:56:40	25.2	13.1	13:02	13:22	2.3	12:11	13:11	1.6
29	20060709	14:00:30			14:02	14:32	–	13:11	14:11	–
30	20060711	00:37:20			00:33	01:03	–	00:03	00:43	–
31	20060711	01:22:30	7.19	7.76	01:23	01:43	1.8	00:43	02:10	–
32	20060713	12:38:10	8.93	5.19		N/A	N/A	12:11	13:11	1.3
33	20060714	21:27:20	24.8	13.5		N/A	N/A	21:24	21:44	1.1
34	20060715	20:07:20	9.91	19.6			N/A	19:11	21:11	1.0
35	20060717	01:29:10	33.2	11.1	01:33	01:43	2.3	00:10	02:10	1.6
36	20060718	00:47:00	10.3	9.72	00:54	01:04	2.0			N/A
CL37	20060718	16:55:50	76.8	7.70	16:54	17:54	1.8	16:11	17:04	1.9
38	20060719	13:20:50			13:24	13:44	1.1?	12:24	13:44	0.97
39	20060723	04:16:10	9.43	4.57	04:07	04:27	1.4	04:11	04:24	0.79
40	20060724	18:39:30	25.6	11.6	18:27	19:07	2.4	18:24	18:44	1.2
41	20060805	16:45:40	24.9	21.3	16:37	17:07	3.2	16:10	17:10	1.8
C?L42	20060805	20:15:20	71.9	7.9			N/A	20:10	21:10	1.5

Table 2: Acronyms used in Table 1

Acronym	Description
$\mathbf{SA_{EQ}}$	Average Spectral Amplitudes of leading earthquake
$\mathbf{SA_{Trem}}$	Average Spectral Amplitudes of tremor
$\mathbf{D_M}$	Mean amplitude of pixel displacements in D_A
im(1,2)	time of image acquisition (internal camera clock)
N/A	no suitable imagery available or noisy results in the DIC analysis
-	No displacments

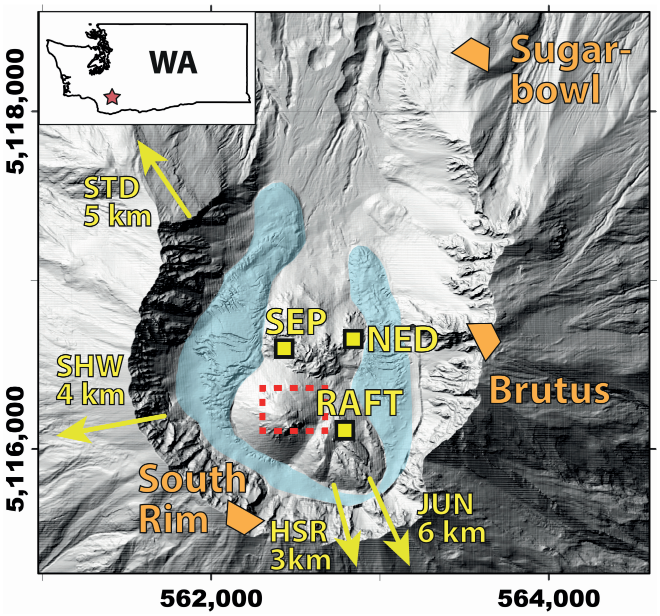

Figure 1: Shaded relief map of the Mount St. Helens summit, based on the USGS National Elevation Dataset (2004) and the August 18, 2006 DEM from *Messerich et al.* [2008]. Locations of the cameras (Sugarbowl, Brutus and South Rim) are shown in orange, the seismometers (VALT, YEL, SEP, RAFT) in yellow. The yellow arrows mark the directions of the seismic stations HSR and SHW at distances of 2.6 km and 3.4 km from the crater center and outside the area covered by this map. The approximate extent of the crater glacier is shaded in blue, the area covered in Figure 10 is marked by the red box.

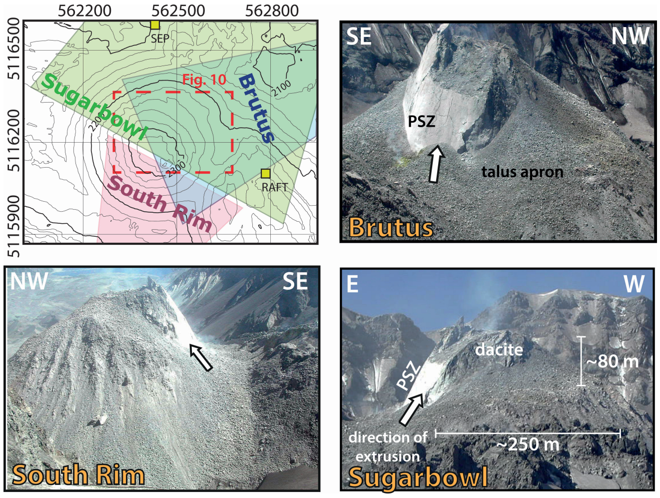

Figure 2: Contour map of dome (25 m intervals) with approximate fields of view of the cameras covered by the original photographs, which were cropped for this figure to show the view on the dome. The striated surface of the exhumed conduit fault is indicated as "Principal Shear Zone" (PSZ), the arrows show the direction of the extrusion in the perspective of the camera. The red box outlines the area covered in Figure 10.

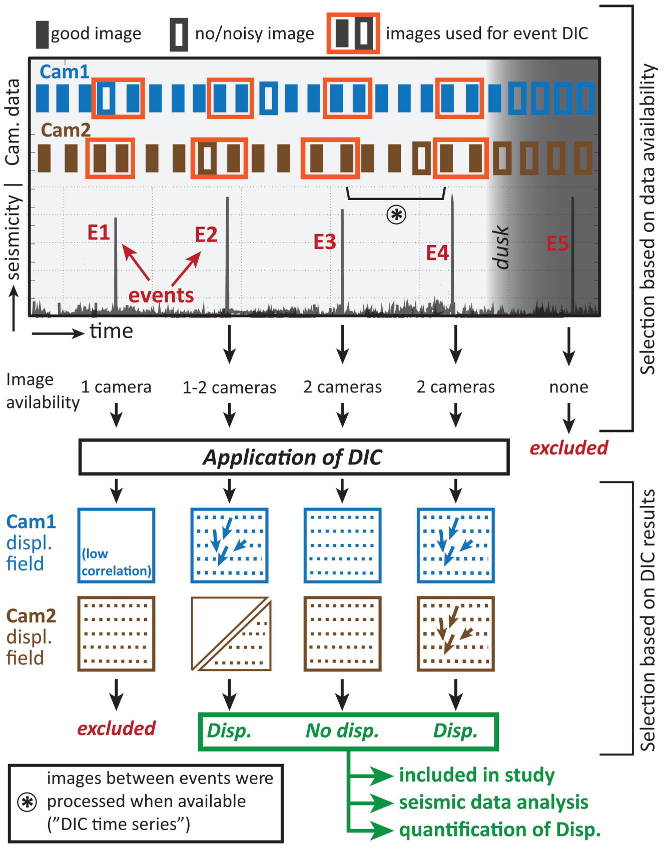

Figure 3: Workflow for compilation of event database illustrated on a schematic seismic and two hypothetical camera datasets (Cam1, Cam2). See text for details.

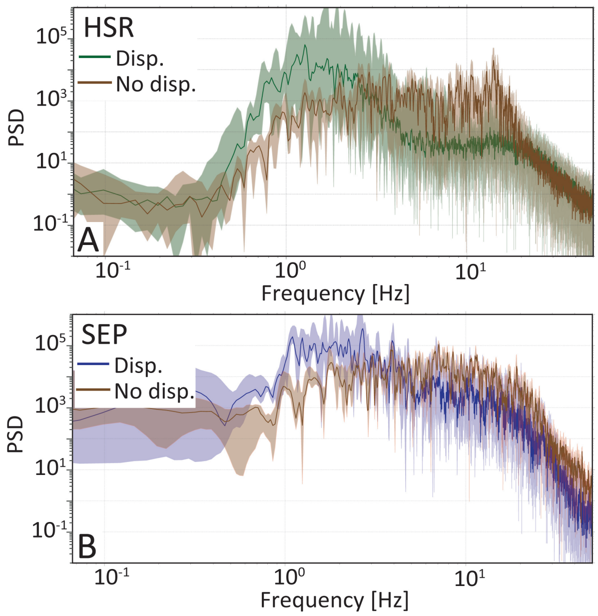

Figure 4: Power Spectral Densities of earthquakes associated and not associated with displacements for the seismic stations HSR (A) and SEP (B). The solid lines show the median PSD, the shaded envelopes correspond to the minimum and maximum values. In order to reduce the contribution of the tremor following the leading earthquake, we only include the first 20 seconds after the onset of the event into the calculation. We used events Ref. 2, 8, 14 and 25 in Table 1 (no displacements) and Ref. 1, 3, 6 and 9 (with displacements), the corresponding waveforms can be found in the appendix.

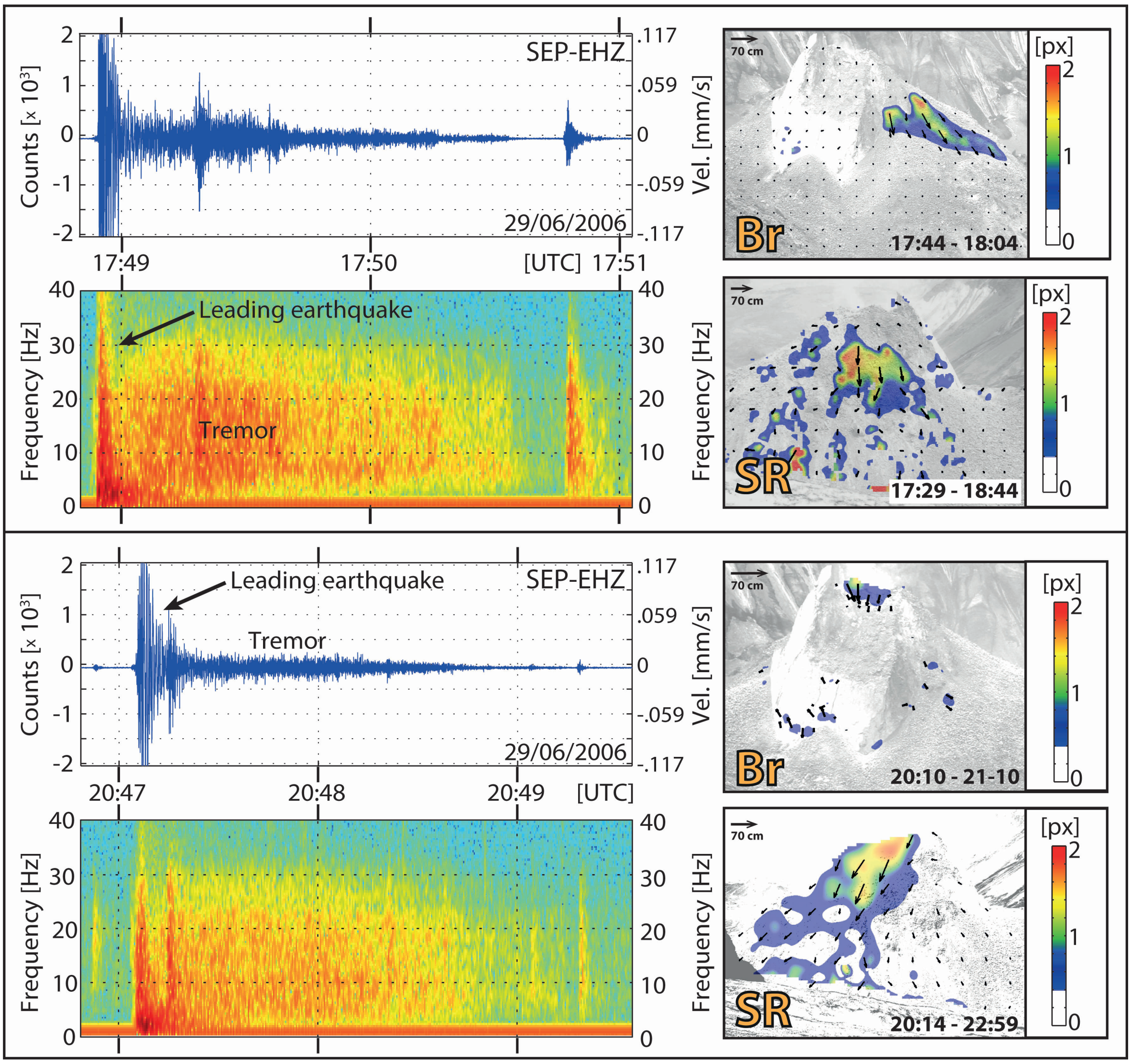

Figure 5: Trace and spectrograms from seismic station SEP showing two examples of events associated with dome displacements (Events Ref. 9 and 11 in Table 1) are shown on the left and the associated pixel displacements calculated from Brutus and South Rim images on the right. An arrow corresponding to 70 cm of displacement along a projected surface orthogonal to the viewing direction of the camera. Note the strong broadband tremor following the main earthquake, and concentration of low frequency energy at beginning of event. Velocities were calculated assuming a flat response.

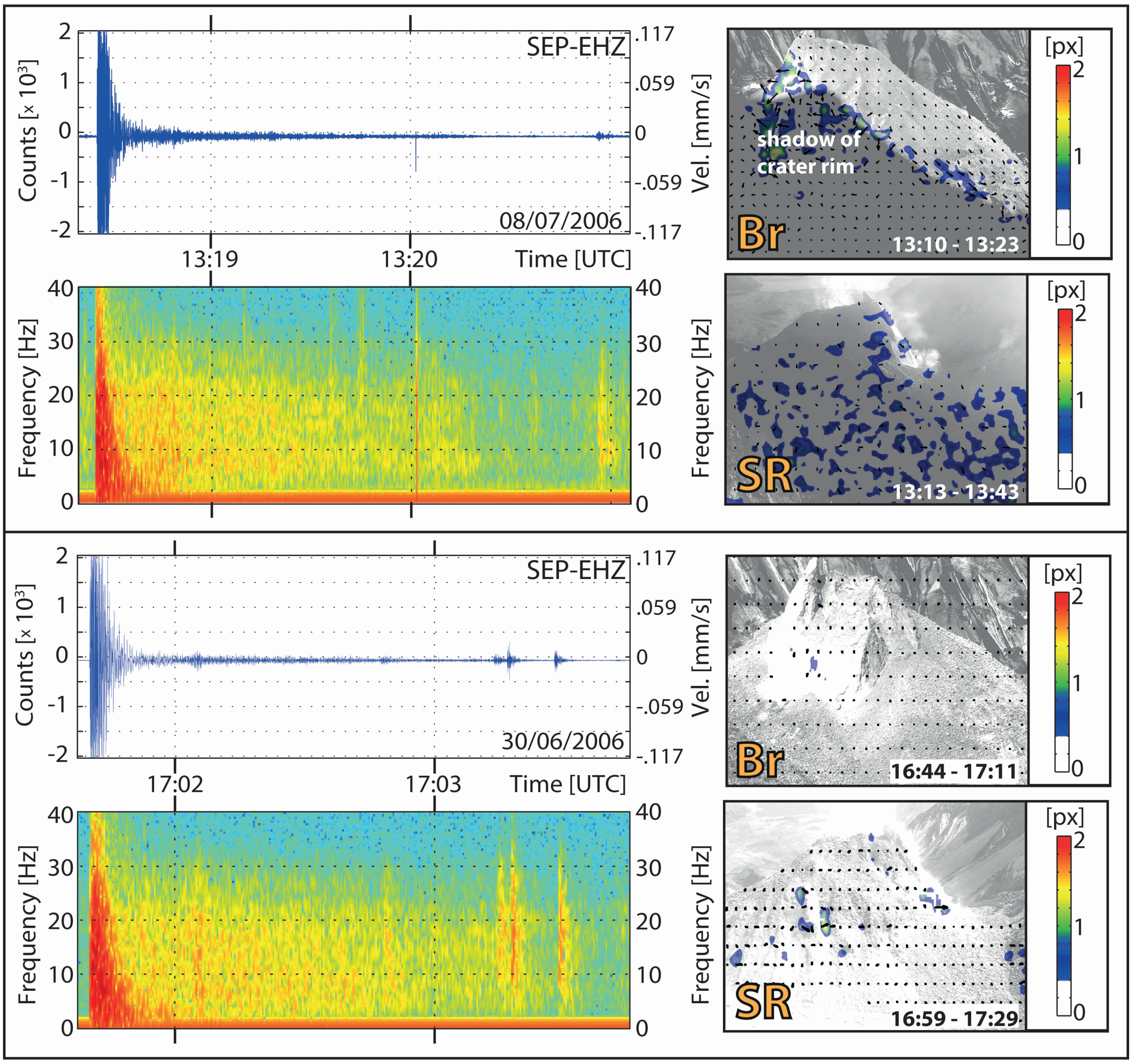

Figure 6: Trace and spectrogram from events lacking displacements (Event Ref. 25 and 14 in Table 1). Note only weak tremor, and lack of low frequency content at the event onset when compared to the events with displacements (Figure 5). Velocities were calculated assuming a flat response.

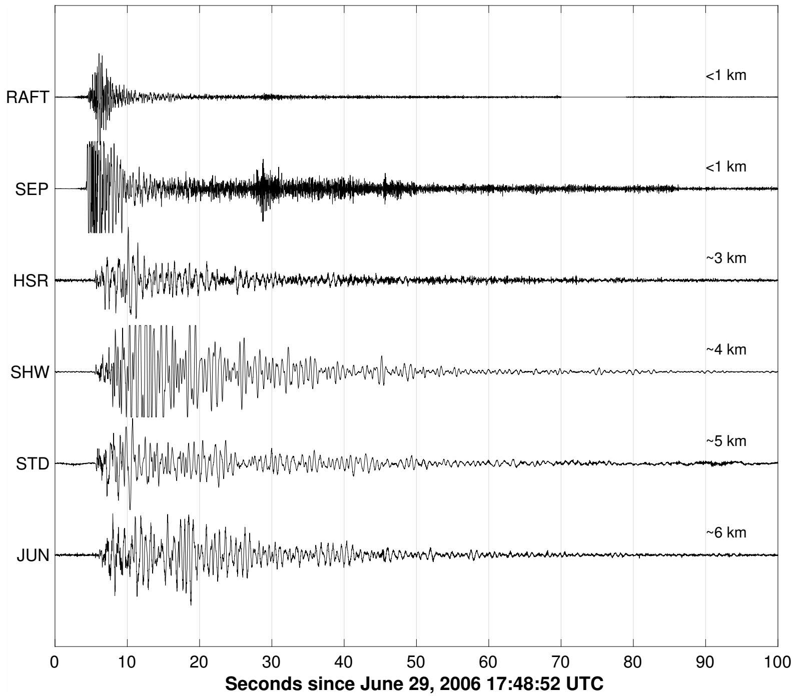

Figure 7: Record section for event Ref. 9 in Table 1. Labels are approximate distances from the source.

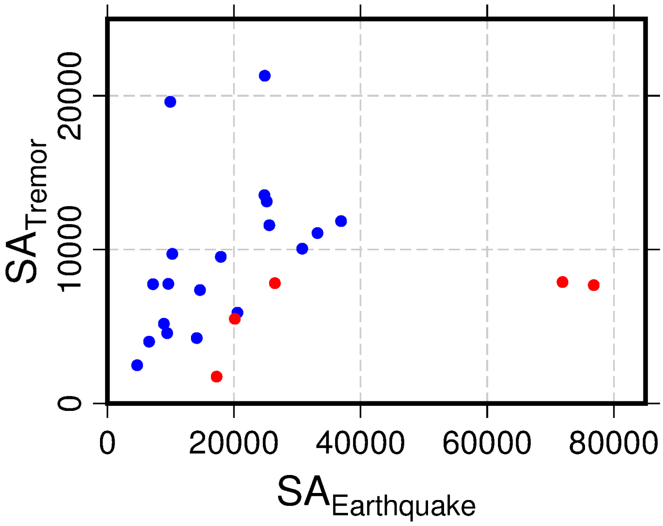

Figure 8: Average spectral values of leading Earthquake Spectral Amplitudes ($SA_{\mathrm{Earthquake}}$) plotted against the tremor Spectral Amplitudes (SA_{Tremor}). Values associated with deformation in the L region are plotted in red.

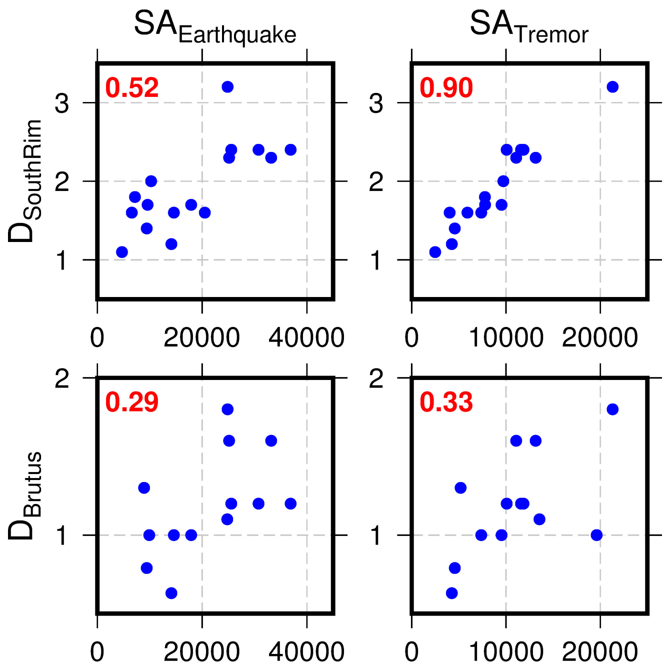

Figure 9: Plots showing relationships between average pixel displacements from Brutus and South Rim cameras (D_{SouthRim} and D_{Brutus}) against Earthquake and Tremor average spectral amplitudes ($SA_{\text{Earthquake}}$ and SA_{Tremor}). The R-square values for a linear fit are plotted in red.

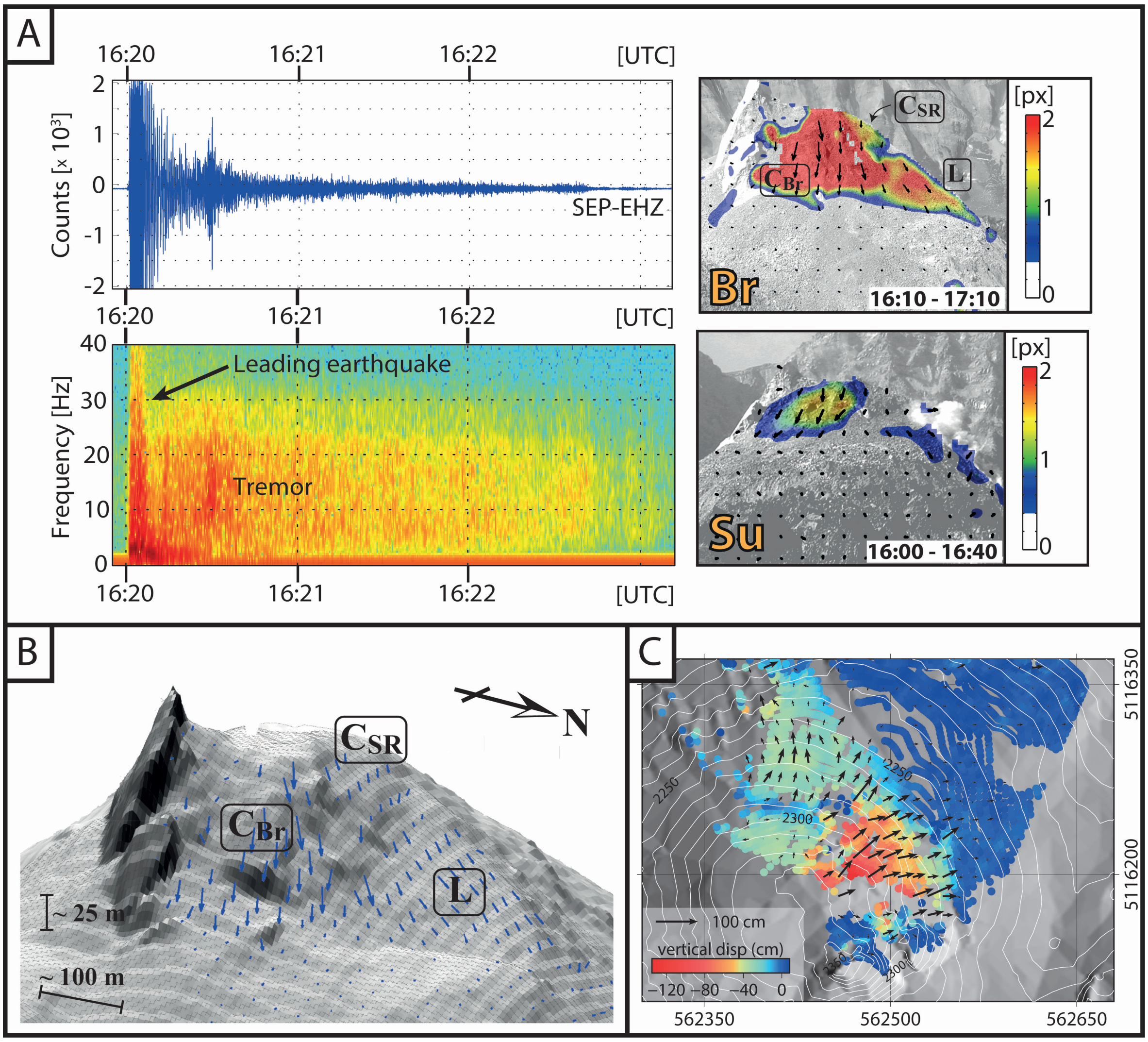

Figure 10: Results of 3D calculations for August 19 event. A.) Traces and spectrogram from SEP station and DIC derived displacement maps from Brutus and Sugarbowl cameras. B.) 3D vectors plotted on the dome topography C.) Top view on the shaded relief. The vertical displacements are plotted in color, the arrows show the horizontal displacements. The labels in red refer to the different dome regions mentioned in the single camera results. C_{Br} = Central region visible from Brutus, C_{SR} = Central region well visible from South Rim, L = lateral region visible from Brutus and Sugarbowl.

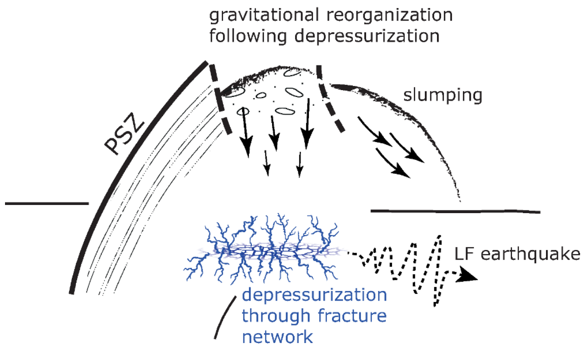

Figure 11: Mechanism based on collapse of pressurized crack or fracture network as driving mechanism for the leading earthquake. Following the evacuation and the low frequency earthquake the overlying dome pile adjusts gravitationally, generating the tremor and highlighting pre-existing internal dome structures. Schematic and not to scale.

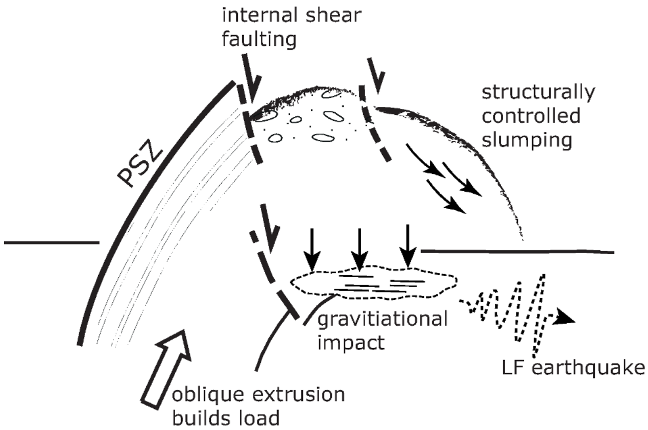

Figure 12: The gravitational load and bending forces resulting from the oblique extrusion may generate the low frequency earthquake by internally collapsing and impacting on the underlying material. The displacements are accommodated by internal shear faulting, and shallow, structurally controlled slumping. Schematic and not to scale.

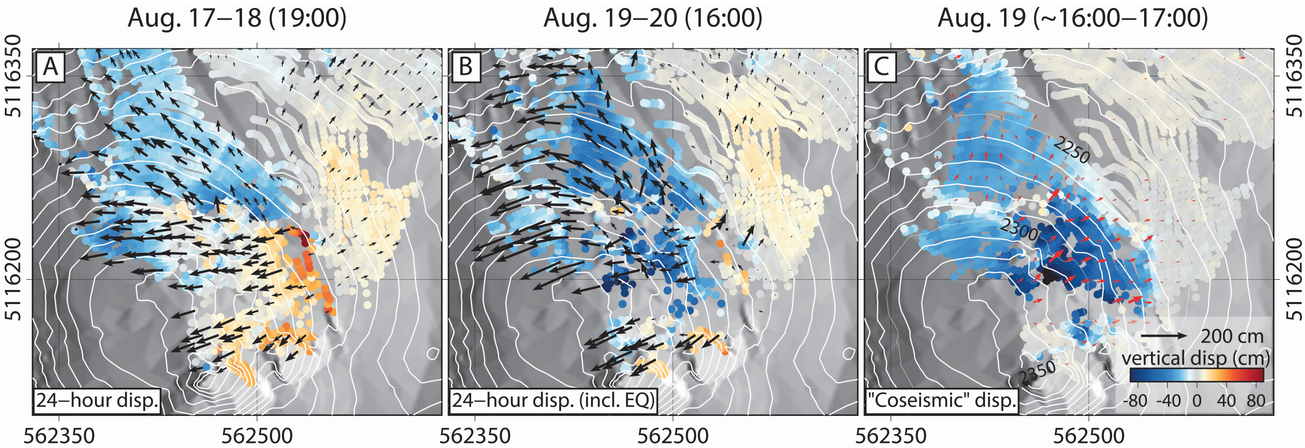

Figure 13: Daily 3D displacements calculated from Brutus and Sugarbowl imagery for Aug. 17-18 (A), Aug. 19-20 (B). The Aug 19-20 displacements also cover the Aug 19 event described in Section 4.4 and also shown (C). Color scale and reference vector for all three panels are given in panel C and are saturated. Contour lines shown at 10 m intervals.